CCS Chemistry

RESEARCH ARTICLE

Received: Sept. 15, 2021 | Accepted: Oct. 27, 2021

Hydrogen-Bonded Dopant-Free Hole Transport Material Enables Efficient and Stable Inverted Perovskite Solar Cells

Rui Li[1†], Chongwen Li[2†], Maning Liu[3], Paola Vivo[3], Meng Zheng[1], Zhicheng Dai[1], Jingbo Zhan[1], Benlin He[2], Haiyan Li[2], Wenjun Yang[1], Zhongmin Zhou[1*] & Haichang Zhang[1*]

[1]Key Laboratory for Rubber-Plastics of Ministry of Education/Shandong Province, School of Polymer Science and Technology, Qingdao University of Science and Technology, Qingdao 266042, [2]Institute of Materials Science and Engineering, Ocean University of China, Qingdao 266100, [3]Hybrid Solar Cells, Faculty of Engineering and Natural Sciences, Tampere University, FI-33014 Tampere

**Corresponding authors: zhouzm@qust.edu.cn; haichangzhang@qust.edu.cn; †*R. Li and C. Li contributed equally to this work.

Cite this: *CCS Chem*. **2021**, *3*, 3309–3319

Although many dopant-free hole transport materials (HTMs) for perovskite solar cells (PSCs) have been investigated in the literature, novel and useful molecular designs for high-performance HTMs are still needed. In this work, a hydrogen-bonding association system (NH···CO) between amide and carbonyl is introduced into the pure HTM layer. Our study demonstrates that the hydrogen-bonding association can not only significantly increase the HTM's hole transport mobility and functionalize the surface passivation to the perovskite layer, but also form Pb–N coordination bonds at the interface to promote the hole extraction while hindering the interfacial charge recombination. As a result, the PSCs based on dopant-free hydrogen-bonded HTMs can achieve a champion power conversion efficiency (PCE) of 21.62%, which is around 32% higher than the pristine PSC without the hydrogen-bonding association. Furthermore, the dopant-free hydrogen-bonded HTMs based device shows remarkable long-term light stability, retaining 87% of its original value after 500 h continuous illumination, measured at the maximum power point. This work not only provides a potential HTM with hydrogen-bonding association in PSCs, but also demonstrates that introducing hydrogen bonding into the materials is a useful and simple strategy for developing high-performance dopant-free HTMs.

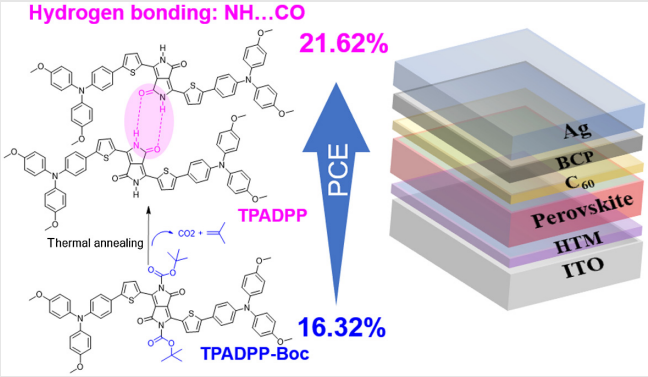

Keywords: hydrogen bonding, dopant-free hole transport material, inverted perovskite solar cell, high efficiency, stability

DOI: 10.31635/ccschem.021.202101483
CCS Chem. **2021**, *3*, 3309–3319

Introduction

The power conversion efficiency (PCE) of perovskite solar cells (PSCs), the leading third-generation low-cost photovoltaic technology, has increased remarkably from 3.8% in 2009 to 25.5% in 2020, which is comparable to that of commercialized crystalline silicon.[1] After light absorption in the PSCs, the generated electrons and holes need to be transported through the perovskite layer and collected at the adjacent charge selective interfaces. A recent report[2] highlights the fact that the performance of PSCs is dominated by swift hole transport (hole injection rate ~1 ns) rather than relatively slow electron transfer (electron injection rate ~11 ns). This suggests that hole transport materials (HTMs) play a key role in the impressive progress of PSCs. Currently, state-of-the-art PSCs with conventional *n*–*i*–*p* structures utilize 2,2′,7,7′-tetrakis(*N*,*N*′-di-*p*-methoxyphenlamine)-9,9-Spirobifluorene (Spiro-OMeTAD) and poly-triarylamine (PTAA) as standard HTMs. However, Spiro-OMeTAD and PTAA are not only tremendously expensive but suffer from low mobility ($<1 \times 10^{-5}$ cm^2 V^{-1} s^{-1}) and limited conductivity ($<3 \times 10^{-7}$ S cm^{-1}).[3] These materials thus need dopants such as bis(trifluoromethane)sulfonimide lithium salt (Li-TFSI) to increase their hole mobility and conductivity that may lead to device degradation due to the (1) sophisticated oxidation process associated with undesired ion migration and (2) chemical interaction with the down-lying perovskite layer.[4] Hence, to overcome the drawbacks of doped HTMs, during the last several years a wide range of novel low-cost dopant-free HTMs have been reported as alternatives to the state-of-the-art HTMs.[5–11]

A good dopant-free HTM is expected to simultaneously display high hole transport mobility and well-matched frontier molecular orbitals (FMOs) with the perovskite valence band edge. Furthermore, to reduce the energy losses at the interface, the HTM needs to passivate the unavoidable defects present in the perovskite layer. In HTMs, holes need to be efficiently transferred within and between individual molecules (intra-/intermolecular conjugation hole transport). To enhance the intramolecular conjugation hole transport, donor–acceptor (D–A) type, D–D type, strong planarity, and large π-conjugation molecular designs have mainly been used for dopant-free HTM.[12–16] Charge-carrier mobility between the adjacent molecules significantly increases if the materials exhibit self-assembling properties that can be exploited to generate ordered structures.[17,18] However, well-organized nanostructures are difficult to obtain with classic solution processing methods due to the disorder packing. Introducing a hydrogen-bonding functionality in the materials, resulting in hydrogen-bonded material superstructures, can be a suitable method to fulfil the above-mentioned critical requirements. Molecules with fused hydrogen-bonding have been reported to exhibit high charge-carrier mobility and conductivity in organic field-effect transistors (OFETs), as demonstrated by our previous work and by other groups as well.[19–23] Materials with high hole mobility in OFETs might be suitable as dopant-free HTMs for PSCs. To the best of our knowledge, there are only two articles that claim the application of hydrogen-bonding functionalized HTMs in PSCs.[24,25] Kaneko et al.[16] proposed small molecular dopant-free HTMs to fabricate *n*–*i*–*p* type PSCs with PCE of 14.5%, but the authors did not focus on the inverted *p*–*i*–*n* structure. In addition, they synthesized the molecules containing multilarge size alkyl chains to enhance the solubility of the small molecules. In most cases, large alkyl-chains result in poor packing and low hole mobility. Later, Más-Montoya et al.[25] synthesized hydrogen-bonded small molecules with no alkyl chain for *p*–*i*–*n* PSCs with PCE of 15.9%, which remained stable for more than 1200 s with a variation of less than 1%. However, due to the poor solubility of the molecules, the device fabrication procedure relied on the thermal evaporation technique, which increases the complexity and cost of the device fabrication. Thus, making dopant-free HTMs by the vapor method cannot be easily and widely used by most research groups (Supporting Information Table S1).

Herein, we report dopant-free D–A–D HTMs with *tert*-butoxylcarbonyl (*t*-Boc)-substituted diketopyrrolopyrrole (DPP) as acceptors, capped at both ends with electron-rich units of triphenylamine (TPA), named TPADPP-Boc. DPP is the most widely used chromophore in OFETs, which enables extremely high hole mobility,[19,26] and TPA is a popular unit to build high-performance HTMs.[27–31] In the designed molecule, the *t*-Boc units could be easily decomposed into carbon dioxide and isobutylene gas upon the thermal annealing process.[32] Meanwhile, the N–H units emerge, and the hydrogen-bonded 3,6-di(5-*N*,*N*-bis(4-methoxyphenyl)aniline-thiophene-2-yl)pyrrolo[3,4-c]pyrrole-2,5(1*H*,4*H*)-dicarboxylate (TPADPP) was formed between the N–H units and the C=O units from the neighboring DPP core (Figure 1). The application of solution-processable hydrogen-bonded dopant-free HTMs is studied in this work. The results showed that hydrogen-bonding association increases the hole mobility of HTMs from 1.11×10^{-4} to 3.09×10^{-4} cm^2 V^{-1} s^{-1}, resulting in a significantly enhanced PCE of PSCs from 16.36% to 21.62% (32% enhancement), which indicates that hydrogen-bonded materials are promising candidates as dopant-free HTMs for efficient PSCs.

Experimental Methods

Synthesis of TPADPP-Boc

TPA-Bo (0.188 g, 0.42 mmol), DPP-Boc-Br (0.131 g, 0.2 mmol), and potassium carbonate aqueous solution (2 M/L 5 mL) were added into freshly distilled toluene

DOI: 10.31635/ccschem.021.202101483
CCS Chem. **2021**, *3*, 3309–3319

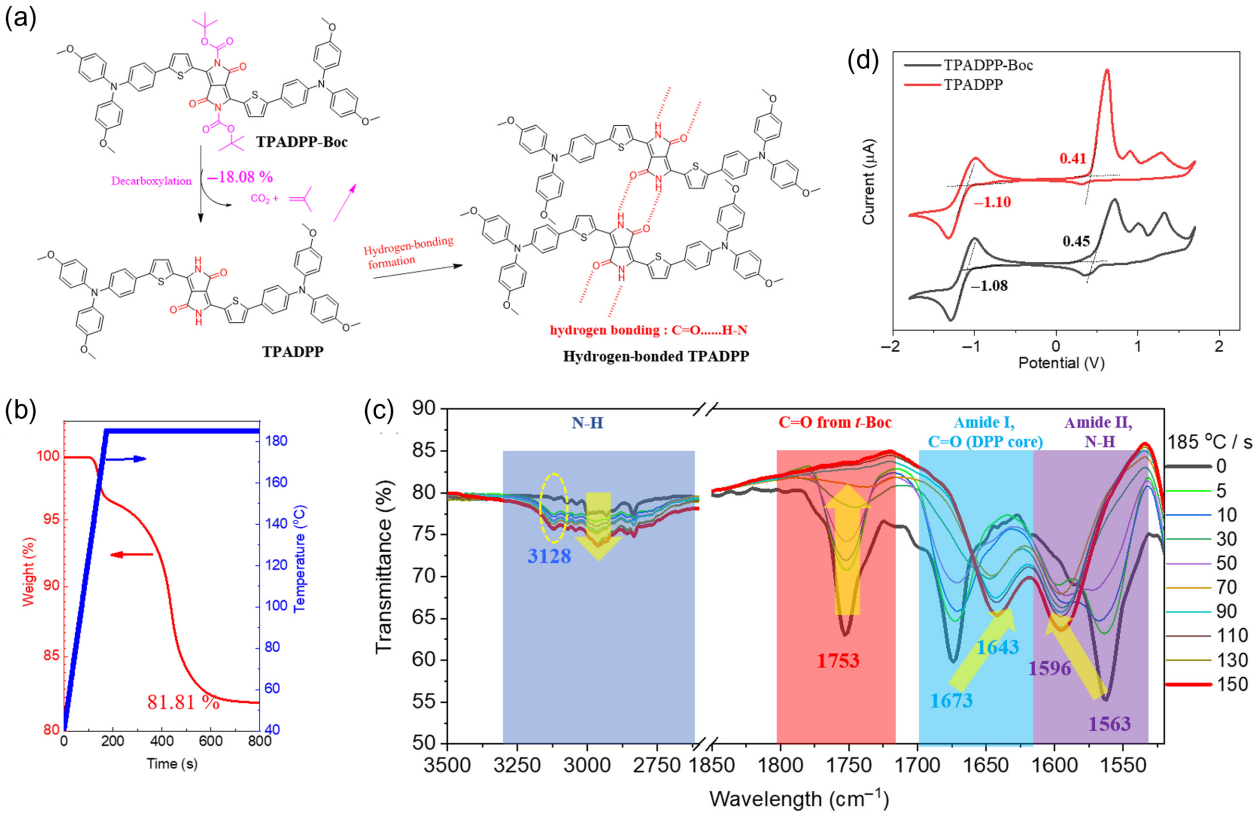

Figure 1 | *(a) Chemical structures of materials, illustration of decarboxylation of PADPP-Boc and hydrogen-bonding formation. (b) TGA spectrum of TPADPP-Boc from room temperature to 185 °C (heating rate 50 °C/min). Once the temperature reached 110 °C, the material was kept at this condition for 800 s. (c) FT-IR spectra of TPADPP-Boc at 185 °C for 150 s. (d) Cyclic voltammograms of the materials as thin films deposited on ITO. Solution: 0.1 M TBAPF$_6$/Acetonitrile. Potentials calculated versus ferrocene. Scan rate: 100 mV s^{-1}; T = 20 °C.*

(15 mL) (Scheme 1). The mixture was degassed with nitrogen, followed by the addition of tetrakis(triphenylphosphine)palladium (0.0115 g, 0.01 mmol). The mixture reacted for 36 h at 100 °C under N_2 protection. After cooling the solution to room temperature, it was extracted with dichloromethane and deionized water twice and dried over anhydrous $MgSO_4$. The crude product was purified by column chromatography (silica gel, dichloromethane) to afford compound TPADPP-Boc as a blue solid (0.195 g, yield: 88%). ^{1}H NMR (500 MHz, d_1-$CHCl_3$, δ) (ppm): 8.31–8.32 (d, 2H), 7.42–7.44 (d, 2H), 7.24–7.25 (d, 2H), 7.08–7.10 (d, 2H), 6.85–6.90 (q, 4H), 3.81 (s, 12H), 1.63 (s, 18H). ^{13}C NMR (125 MHz, d_1-$CHCl_3$, δ) (ppm): 159.31, 156.44, 151.67, 149.56, 149.14, 140.02, 136.71, 135.74, 127.16, 126.97, 124.63, 122.72, 119.50, 114.85, 109.62, 85.71, 55.51, 55.45, 27.75. Microanalysis found C, 69.45%; H, 5.27%; N, 5.05%; S, 5.79% (C, 69.42%; H, 5.28%; N, 5.06%; S, 5.79%).

Synthesis of TPADPP

TPADPP-Boc (0.055 g, 0.05 mmol) was thermally annealed on a hot plate at 185 °C for 10 min (Scheme 2). The dark blue product of TPADPP was obtained (0.045 g,

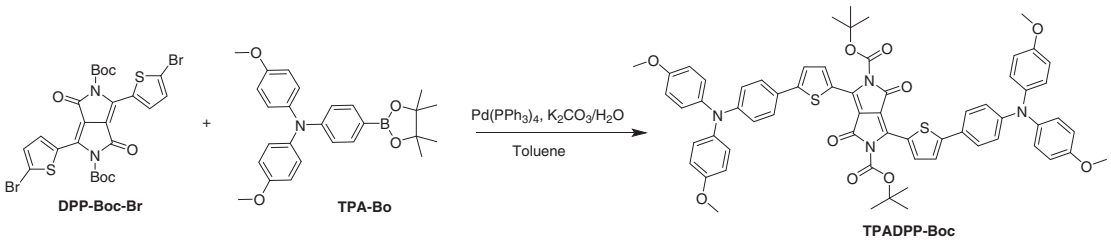

Scheme 1 | *Synthetic route of TPADPP-Boc. The synthesis route and NMR spectrum of the starting product of TPA-DPP are shown in Supporting Information Figures S9–S13 and Schemes S1–S4.*

DOI: 10.31635/ccschem.021.202101483
CCS Chem. **2021**, *3*, 3309–3319

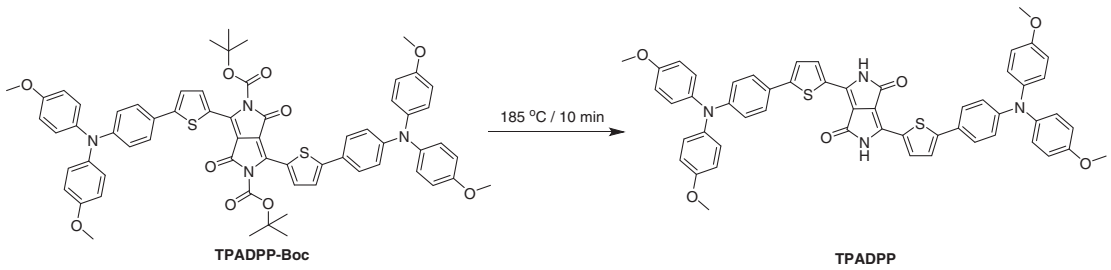

Scheme 2 | *Synthetic route of TPADPP.*

yield: 100%). Due to the poor solubility of the TPADPP, the NMR spectra were not measured. Microanalysis found C, 71.49%; H, 4.69%; N, 6.18%; S, 7.05% (C, 71.50%; H, 4.67%; N, 6.18%; S, 7.07%).

Perovskite ($FA_{0.8}Cs_{0.2}PbI_{2.96}Br_{0.04}$) solution

The 1.35 M $FA_{0.8}Cs_{0.2}PbI_{2.96}Br_{0.04}$ perovskite precursor solution was obtained by dissolving 137.6 mg of formamidinium iodide, 52 mg of cesium iodide, 447.2 mg of lead iodide, 11 mg of lead bromide, and 5.2 mg of lead thiocyanate in a mixed solvent of *N*,*N*-dimethylformamide and dimethyl sulfoxide with a ratio of 3:1. The precursor solution was stirred at 60 °C for 3 h before use.

Device fabrication

The indium-doped tin oxide (ITO) glass substrates with an optical transmission of >80% in the visible range and sheet resistance of 8–10 Ω^{-2} were purchased from Techno Print Co., Ltd. (Chiba, Japan). The patterned ITO substrate was first cleaned using a surfactant, then washed with sequential sonication in deionized water, ethanol, and acetone for 10 min, respectively. Finally, it was subjected to UV/ozone treatment for 30 min before utilization. The HTM layers were fabricated by spin-coating them at 3000 rpm for 30 s, then annealing at 100 and 180 °C for 10 and 30 min, respectively. The perovskite films were prepared by dripping 100 μL of the perovskite precursor solution on substrates followed by spin-coating at 500 rpm for 2 s and 4000 rpm for 50 s. 750 μL of diethyl ether was dripped at the 25th second of the second step. Then the films were transferred to a preheated hot plate at 65 °C for 2 min and then to a 100 °C hot plate for 15 min. After the formation of the perovskite film, the C_{60} electron transporting layer (30 nm) and 2,9-Dimethyl-4,7-diphenyl-1,10-phenanthroline (BCP) hole-blocking layer (10 nm) were evaporated successively. A 100 nm thick of Ag cathode was thermally evaporated under a reduced pressure of 2×10^{-5} Torr to achieve a complete device via a metal shadow mask of 0.094 cm^2.

Results and Discussion

Design and synthesis of the TPA-DPP

Figure 1 shows the molecular structure of TPADPP-Boc. The synthetic route to the target TPADPP-Boc was straightforward via the Suzuki coupling reaction between dibromominated DPP and 4-broate ester-4-*N*,*N*-bis(4-methoxyphenyl)aniline (TPA-Bo) (see Supporting Information). Compared to PTAA or Spiro-OMeTAD HTMs, the cost of the TPADPP-Boc is significantly lower ($12.69/g) (Supporting Information Tables S2–S8). The two *t*-Boc units of the TPADPP-Boc enable good solubility in most common organic solvents, rendering their solutions processable. Upon thermal annealing, the *t*-Boc units were decomposed, while the TPADPP-Boc was converted into TPADPP. TPADPP contains two lactam units that can form intermolecular hydrogen-bonding pairs (NH···OC, Figure 1a).[23] To validate the formation of the TPADPP with fused hydrogen bonding after the decarboxylation of the *t*-Boc groups, thermogravimetric analysis (TGA), elemental analysis, and Fourier transform infrared (FT-IR) experiments were conducted. As shown in Figure 1b, the TPADPP-Boc decomposed under 185 °C heating for 10 min with a weight loss of around 18.19%, which matched well with the weight percentage of the *t*-Boc units in TPADPP-Boc (18.08%). In addition, the elemental analysis of the annealed TPADPP-Boc matched well with the TPADPP element composition. These observations indicate that the *t*-Boc units could be easily decomposed through the thermal annealing process and the TPADPP-Boc converted into TPADPP.

To further confirm the formation of the hydrogen bonding between the neighboring TPADPP molecules in the thin film, the FT-IR spectra were measured under 185 °C for varied periods. As can be seen from Figure 1c, during the thermal annealing at 185 °C for 150 s, the absorption peak at 1753 cm^{-1} (C=O stretching of *t*-Boc units) gradually decreased and finally disappeared, which can be ascribed to the decarboxylation. Meanwhile, the *N*-Boc units changed into N–H groups. Once the N–H group emerged, the hydrogen-bonding association was formed between the N–H units and the C=O units from the neighboring

DOI: 10.31635/ccschem.021.202101483
CCS Chem. **2021**, *3*, 3309–3319

TPADPP. This led to the following observations: (1) A broad absorption peak between 2700 and 3255 cm^{-1} emerged, typically the peak located at 3128 cm^{-1}, which is ascribed to the hydrogen-bonded NH stretching vibration. (2) The absorption peak of the carbonyl group from the DPP core located at 1673 cm^{-1} was shifted to 1643 cm^{-1}, indicating that the isolated C=O groups were bonded with NH units (C=O···H–N). (3) The amide I signal shifted to lower wavenumbers (C=O stretching, from 1673 to 1643 cm^{-1}), while the amide II signal shifted to higher wavenumbers (N–H bending, from 1563 to 1596 cm^{-1}), which consequently confirmed the formation of a secondary amine.[33–36] The FT-IR results agreed well with those reported for published hydrogen-bonded systems.

The UV–vis absorption spectra of both molecules in the thin-film state are shown in Supporting Information Figure S1. Both materials exhibited two absorption peaks between 590 and 665 nm. After the decarboxylation, the peaks were significantly red-shifted by 25 nm, which could be ascribed to the fact that the hydrogen-bonding association in the TPADPP thin film resulted in strong aggregation.[17] From the absorption onset, the optical bandgaps of 1.68 eV for TPADPP-Boc and 1.52 eV for TPADPP were estimated (Supporting Information Table S9). The electrochemical properties of the materials were studied using cyclic voltammetry (CV) and ultraviolet photoelectron spectroscopy (UPS). From the onsets of anodic oxidation and cathodic reduction, the highest occupied molecular orbital (HOMO) and lowest unoccupied molecular orbital (LUMO) energy levels of TPADPP-Boc were calculated as –5.25 and –3.72 eV, while the TPADPP showed slightly higher HOMO energy levels (–5.21 eV) and lower LUMO energy levels (–3.70 eV, Figure 1d). The high HOMO energy levels of the two materials can be ascribed to the strong electron donor character of bis(4-methoxyphenyl)amine. The HOMO energy levels calculated from CV curves matched well with the results obtained by UPS (–5.25 and –5.20 eV for TPADPP-Boc and TPADPP, respectively, Supporting Information Figure S2). The FMO energy levels of the two molecules were higher than the valence band of the perovskite, indicating that the two materials are potentially suitable as HTMs for only transferring the holes while blocking the electron transfer from the perovskite layer to HTM layers.

Device properties

To build an efficient PSC device, the morphology, quality, and contact angle of the HTMs thin films should be carefully considered. The surface morphology of the HTMs was characterized by atomic force microscopy (AFM). The TPADPP-Boc film was annealed at 110 °C for 10 min to remove the residual chlorobenzene. Under this condition, the TPADPP-Boc exhibited thermally stable properties (Supporting Information Figure S3). To get rid of the two Boc groups and obtaining the TPADPP-Boc film, further thermal treatment under 185 °C for 10 min was used. As shown in Figures 2a and 2b, both film surfaces were fully covered by the HTMs. However, the TPADPP film showed lower roughness and was more uniform than the TPADPP-Boc film. Generally, the perovskite materials are difficult to deposit on organic HTM layers, due to their low wettability. To check the wettability of both films, the contact angles of both films were measured. Figures 2c and 2d show that the TPADPP film exhibits a much lower contact angle than TPADPP-Boc (TPADPP-Boc: 92°; TPADPP-61°), indicating the ease of perovskite film deposition. This might be ascribed to the fact that, after removing the Boc units, the NH functional groups, which are more hydrophilic, emerged.

High hole transport mobility plays a key role in designing high-performance dopant-free HTMs. Normally, HTMs would not need additional doping process if they exhibit hole mobilities up to $10^{-3} \sim 10^{-4}$ cm^2 V^{-1} s^{-1}.[37] In this work, the charge transport properties of both films with and without Boc groups were evaluated by utilizing the space-charge-limited-current (SCLC) method.[38] The dark *I*–*V* characteristics of the hole-only devices with configuration 'ITO/poly(3,4-ethylenedioxythiophene) (PEDOT): poly(styrenesulfonate) (PSS)/hole transport layer (HTL)/Ag' were evaluated (Figure 2e). The hole mobilities were extracted by the Mott–Gurney Law (1):

$$\mu = \frac{8J_D L^3}{9\varepsilon_0 \varepsilon_r V^2} \quad (1)$$

where ε_0 is the vacuum permittivity, ε_r is the relative dielectric constant (assuming $\varepsilon_r = 3$ for organic materials), L is the thickness of HTM, J_D is the dark current density, and V is the applied voltage. The determined thickness of both films under optimal concentration was 20 nm. As a result, the hole mobilities of the films with and without Boc groups were calculated as 1.11×10^{-4} and 3.09×10^{-4} cm^2 V^{-1} s^{-1}, respectively, compared to 6.94×10^{-4} cm^2 V^{-1} s^{-1} of classic PTAA (Supporting Information Figure S4). This indicates that both pristine films can efficiently perform as hole transport materials in PSCs. Compared to TPADPP-Boc, the hole transport mobility of TPADPP was enhanced by almost three times, which can be ascribed to the hydrogen-bonding formation.

Scanning electron microscopy (SEM) was used to characterize the surface morphology of the perovskite films atop the HTMs with and without Boc groups. As shown in Figures 3a and 3b, both perovskite films are uniform and fully covered to prevent direct contact with the cathode and anode and in turn eliminating current leakage.[39] Besides, there is no discernible thickness change of perovskite films, as shown in Supporting Information Figure S5. Figure 3c shows the UV–vis absorption spectra of the perovskite samples. The absorption of both the perovskite films is almost the same at 780 nm, which can be attributed to the similar size and thickness of the perovskite grains. To investigate the influence of the HTMs with and

DOI: 10.31635/ccschem.021.202101483
CCS Chem. **2021**, *3*, 3309–3319

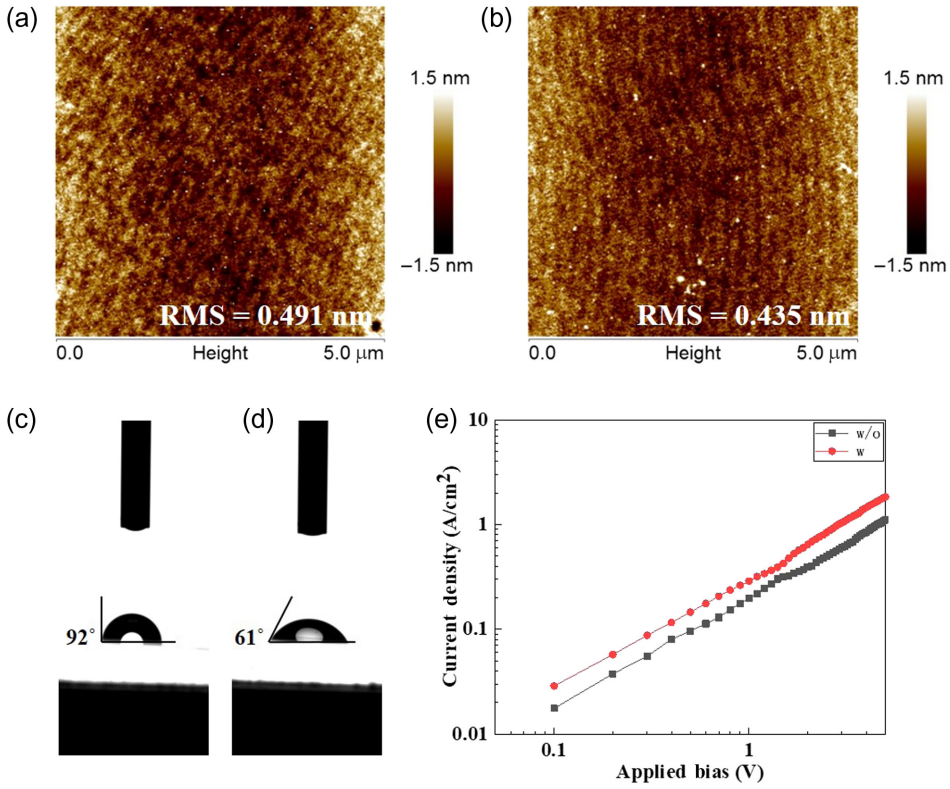

Figure 2 | *AFM images of (a) TPADPP-Boc and (b) TPADPP thin films on ITO. Contact angles of (c) TPADPP-Boc and (d) TPADPP films with respect to water droplets. (e) The SCLC measurements of hole-only devices with configuration "ITO/PEDOT:PSS/HTM/Ag".*

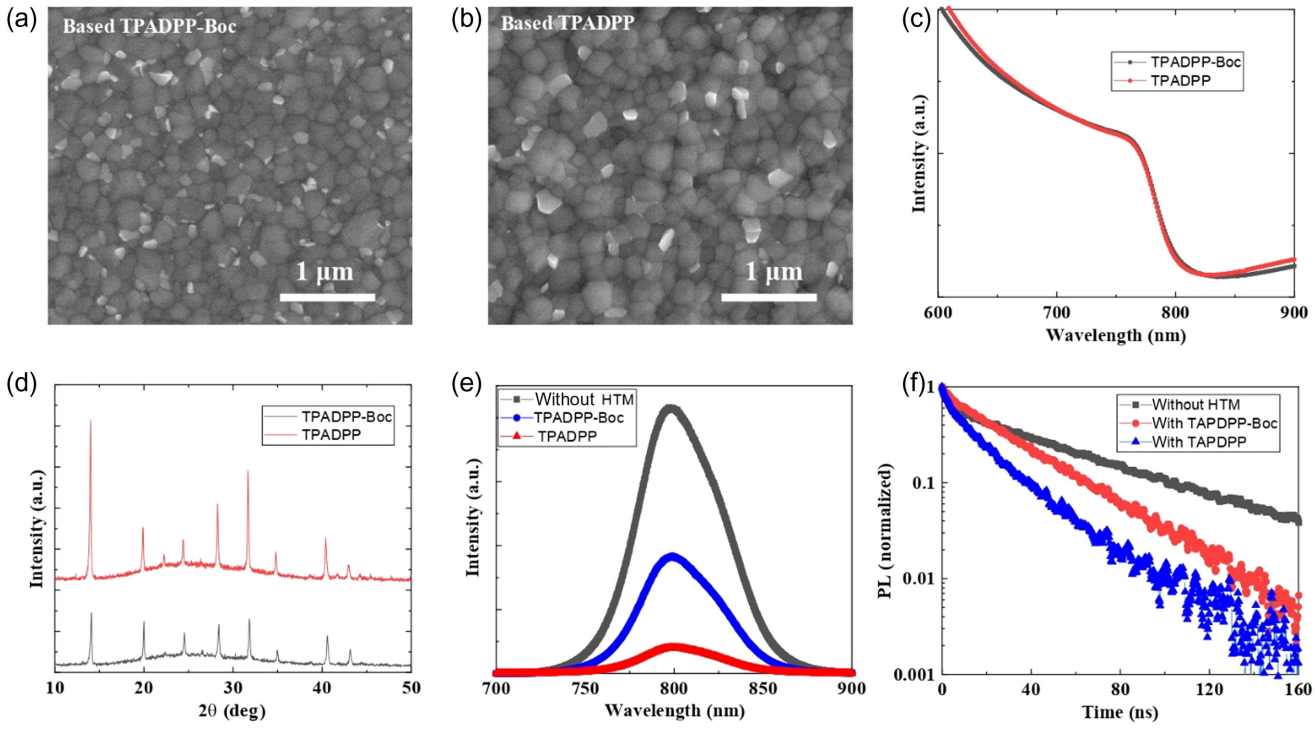

Figure 3 | *Top-view SEM images of perovskite films based on (a) TPADPP-Boc and (b) TPADPP. (c) UV–vis absorption spectra. (d) XRD pattern spectra. (e) Steady-state PL spectra. (f) TRPL decay transient spectra.*

DOI: 10.31635/ccschem.021.202101483
CCS Chem. **2021**, *3*, 3309–3319

without Boc groups on the crystallinity of perovskite films, the X-ray diffraction (XRD) analysis was performed. As shown in Figure 3d, the 2θ angle of all diffraction peaks of the perovskite films, which are independent on the underlayer, is consistent with the previous reports. Both perovskite films showed strong diffraction peaks at 14.11° with full width at half maxima (FWHM) of 0.149° for TPADPP and 0.167° for TPADPP, respectively, which is assigned to the (100) planes. The higher peak of perovskite deposited on the TPADPP film at 14.11° demonstrates its better crystallinity and more effective charge transport along the *z*-axis compared to the perovskite deposited on the TPADPP-Boc film. This might be ascribed to the fact that, after removing the Boc units, the NH groups emerged and passivated the perovskite surface.

After the light absorption, the generated holes need to be transported through the perovskite layer and collected at the adjacent HTM layer. This step plays a key role in achieving high-performance PSCs. To investigate the interfacial hole extraction process at the interface between the perovskite and HTM, steady-state and time-resolved photoluminescence (TRPL) measurements were conducted. Figure 3e shows a clearly enhanced PL quenching when depositing a perovskite film on the TPADPP layer compared to the case of perovskite atop the TPADPP-Boc layer. The calculated quenching efficiencies, that is, hole extraction efficiencies, are 58.4% and 91.0% for TPADPP-Boc and TPADPP, respectively. This suggests that the NH groups of TPADPP can form Pb–N coordination-bonds through the formation of Lewis adducts between under-coordinated Pb atoms and N atoms at the perovskite/HTM interface, which can significantly promote interfacial hole extraction.[40] The hole extraction dynamics were also monitored by comparing the TRPL decays in Figure 3f. A clear decay acceleration was observed for glass/perovskite/TPADPP compared to glass/perovskite/TPADPP-Boc, indicating that the holes at the perovskite/HTM interface can be swiftly extracted with the help of the Pb–N bond, which is highly consistent with PL quenching data. We then attempted to quantitatively analyze the PL decay data by using a reported kinetic model, that is, a one-dimensional charge diffusion model (see the analysis method in Supporting Information).[41,42] A rate equation (see Supporting Information Equation S1) was used to fit the PL decay data, including first-order recombination (k_1) via carrier traps, second-order nongeminate-free charge carrier (electron and hole) recombination (k_2), and interfacial hole extraction process (k_{HT}). The resulting k_1, k_2, and k_{HT} for two HTMs are summarized in Supporting Information Table S9. TPADPP exhibited reduced k_1 (8.5×10^6 s^{-1}) and k_2 (1.3×10^{-10} s^{-1} cm^3) compared to those ($k_1 = 2.3\ 10^7$ s^{-1} and $k_2 = 4.1 \times 10^{-10}$ s^{-1} cm^3) of TPADPP-Boc, suggesting that the interfacial Pb–N bond not only promotes hole extraction but also hinders single-carrier trapping recombination by filling the surface traps of the perovskite. Moreover, the hole extraction rate constant (k_{HT} = 5.4×10^8 s^{-1}) of TPADPP was nearly one order of magnitude higher than that (6.1×10^7 s^{-1}) of TPADPP-Boc, which is also evident by the faster effective lifetime ($\tau_{1/e}$ = 11.5 ns) of TPADPP-based film compared to that ($\tau_{1/e}$ = 24.7 ns) of TPADPP-Boc case (see Supporting Information Table S9). To investigate the PSC performance based on the designed HTMs, the *p–i–n* configuration of ITO/HTM/Perovskite/C_{60}/BCP/Ag (Figure 4a) PSCs with an active area of 0.094 cm^2 was realized. Figure 4b shows the energy-level alignment of each layer of the device. The optimal thickness of the HTM, evaluated by comparing the device performance with varying concentrations of TPADPP solutions (Supporting Information Figure S6), was ~20 nm. Figure 4c shows the current density–voltage (*J–V*) curves (measuring under AM 1.5G illumination at 100 mW cm^{-2}) of the champion device with negligible hysteresis. TPADPP-based PSC exhibits an open-circuit voltage (V_{OC}) of 1.115 V, a short-circuit current density (J_{SC}) of 23.27 mA cm^{-2}, a fill factor (FF) of 0.833, and a PCE of 21.62% under the reverse-scan direction. The parameters of this champion device under the forward-scan direction include a V_{OC} of 1.118 V, a J_{SC} of 23.24 mA cm^{-2}, an FF of 0.818, and a PCE of 21.26%. This indicates the TPADPP is a promising dopant-free HTM. For the comparison of the hydrogen-bonding association of HTM on the performance of the PSC, the device with TPADPP-Boc film as HTM was fabricated, and the corresponding *J–V* curves are also shown in Figure 4c. Table 1 summarizes the photovoltaic parameters of the devices with TPADPP and TPADPP-Boc as HTMs, respectively. After removing the Boc units from the HTM structure, the V_{OC} and J_{SC} of the corresponding PSCs were significantly enhanced, which resulted in a PCE boost from 16.36 up to 21.62% (32% enhancement). Such a significant performance improvement can be ascribed to the following: (1) The hydrogen-bonding association for the HTMs improves the hole transport mobility within the HTM layer. (2) The NH units passivate the perovskite surface, leading to a perovskite layer with good quality and crystallinity. (3) The NH groups form Pb-N coordination bonds between the top-coordinated Pb atoms at the interface, which can significantly improve the hole extraction rate.[28] In this work, the *p–i–n* PSCs, employing a hydrogen-bonded dopant-free HTM, achieved a champion PCE of 21.62%, which is comparable with the recent highest PCE records.[43]

The integration of the external quantum efficiency (EQE) spectra of the champion devices based on the hydrogen-bonded TPADPP, TPADPP-Boc, and PTAA HTMs, yielded the photocurrent densities of 22.1, 21.3, and 22.7 mA/cm^2, respectively, which are consistent with the measured J_{SC} (Figure 4d). To check the device reliability, the PSCs based on TPADPP, TPADPP-Boc, and PTAA were tested with the photocurrent output under a fixed bias. As presented in Figure 4e, there are stable photocurrent densities and efficiency outputs for the devices with

DOI: 10.31635/ccschem.021.202101483
CCS Chem. **2021**, *3*, 3309–3319

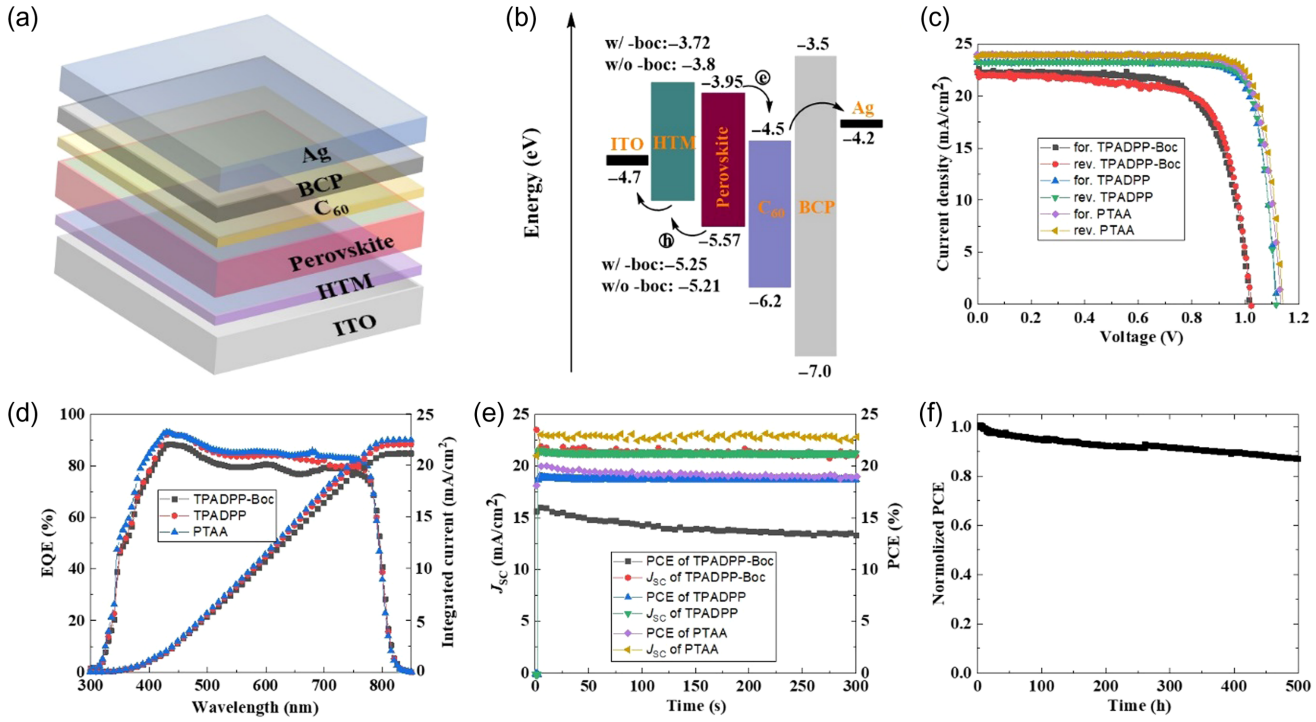

Figure 4 | *(a) Illustration of the device structure. (b) Energy-level diagram for the device. (c) J–V curves of PSCs with TPADPP-Boc, TPADPP, and PTAA HTMs under illumination of AM 1.5G 100 mW cm^2. (d) EQE curves of PSCs with TPADPP-Boc, TPADPP, and PTAA HTMs. (e) Maximum steady-state photocurrent output of the champion device at the MPP. (f) Long-term stability tests of devices based on TPADPP under light soaking at MPP (1 sun, with 420 nm UV light cutoff filter; 35 °C; bias potential 0 V; using glass lid/UV epoxy encapsulation) and under storage conditions.*

TPADPP and PTAA as HTMs compared to those based on TPADPP-Boc over a period of 300 s under a continuous AM 1.5G illumination. To further quantitatively estimate the defects density in a perovskite, the SCLC method with the device structure 'ITO/HTM/Perovskite/Spiro-OMeTAD/Au' was exploited. The *J–V* curves were obtained in the dark. As shown in Supporting Information Figure S7, the trap-filled voltage (V_{TFL}) was obtained through a kink point between the ohmic and the trap-filled regimes. The defects density (N) was calculated based on the following eq 2[44]:

$$V_{TFL} = \frac{eNL^2}{2\varepsilon\varepsilon_0} \quad (2)$$

where e is the elementary charge, L is the thickness of perovskite film, ε is the relative dielectric constant of the perovskite, and ε_0 is the vacuum permittivity. The defect density was calculated as 1.22 × 10^{16}, 5.88 × 10^{15}, and 4.27 × 10^{15} cm^{-3} for the devices based on the TPADPP-Boc, TPADPP, and PTAA, respectively, which revealed that the perovskite film deposited on TPADPP film showed much lower defect density than the perovskite deposited on TPADPP-Boc film. This further indicates that the NH units of the TPADPP core can passivate the perovskite surface.

Long-term device stability is one of the most important challenges for the emerging PSC technology. In this work, the stability of the PSC based on hydrogen-bonded TPADPP materials was measured at maximum power point (MPP) under continuous illumination at 100 mW cm^{-2} (Figure 4f). In addition, we investigated the illumination-time dependence on the decay of two key photovoltaic

Table 1 | *Photovoltaic Parameters (Average and Maximum Values) of 15 Separated Devices Based on the HTMs with and without Boc, Respectively*

HTM		V_{OC}/V	J_{SC}/mA cm^{-2}	FF	PCE
With Boc	Ave.	0.98 ± 0.04	24.02 ± 0.78	0.67 ± 0.02	15.74 ± 0.53
	Max.	1.02	22.22	0.72	16.36
Without Boc	Ave.	1.11 ± 0.01	23.80 ± 0.29	0.79 ± 0.02	20.89 ± 0.65
	Max.	1.12	23.27	0.83	21.62

DOI: 10.31635/ccschem.021.202101483
CCS Chem. **2021**, *3*, 3309–3319

parameters (J_{sc} and V_{oc}). The device maintained 87% of its initial PCE value after 500 h. There is no significant change in V_{oc} during the illumination time (Supporting Information Figure S8). However, we could observe a gradual drop in J_{sc}, which may be caused by the degradation of the perovskite layer due to ion migration.

Conclusion

Two D–A–D typed materials, namely TPADPP-Boc and TPADPP, were designed, synthesized, and applied in the PSCs as dopant-free HTMs. TPADPP was obtained via the thermal annealing of TPADPO-Boc. Our studies showed that, after the decarboxylation, the N-Boc units were converted to NH groups, which then formed hydrogen-bonding (NH···CO) with the carbonyl of the neighbouring DPP core. The hydrogen-bonding association significantly enhanced hole transport mobility—up to 3.09×10^{-4} $cm^2 V^{-1} s^{-1}$ for TPADPP—which is three times higher than that of TPADPP-Boc. Furthermore, the NH units that emerged could not only passivate the surface of the perovskite layer for a more crystalline perovskite film but also form Pb–N coordination bonds at the interface between the HTM and the perovskite layer, which significantly improve the hole extraction. As a result, the dopant-free hydrogen-bonded TPADPP based PSCs achieved a champion PCE of 21.62%, which bears comparison with that of classical doped PTAA-based devices (PCE around 22%). However, the pristine PSC based on TPADPP-Boc showed a PCE of only 16.36%. Furthermore, the dopant-free TPADPP-based device showed remarkably high long-term photostability, retaining 87% of its original value after 500 h of continuous illumination measured at MPP. Introducing hydrogen bonding in the molecular design concept, such as amine units, is a simple and useful strategy to develop high-performance solution-processed dopant-free HTMs. This study is expected to provide a guideline for further development of dopant-free HTMs for highly efficient and stable inverted PSCs.

Supporting Information

Supporting Information is available and includes experimental procedures, Figures S1–S13, and Tables S1–S10.

Conflict of Interest

The authors declare no conflict of interest.

Funding Information

This research was made possible as a result of a generous grant from the Natural Science Foundation of China (grant no. 21805151), the Natural Science Foundation of Shandong Province, China (grant no. ZR2018MB024), and the Young Taishan Scholars (grant nos. 201909120 and 201909121). M.L. acknowledges the Finnish Cultural Foundation (no. 00210670) for funding. P.V. thanks the Jane and Aatos Erkko foundation (project ASPIRE) for financial support. This work is part of the Academy of Finland Flagship Programme, Photonics Research and Innovation (PREIN), Decision No. 320165.

References

1. Kojima, A.; Teshima, K.; Shirai, Y.; Miyasaka, T. Organometal Halide Perovskites as Visible-Light Sensitizers for Photovoltaic Cells. *J. Am. Chem. Soc.* **2009**, *131*, 6050–6051.
2. Makuta, S.; Liu, M.; Endo, M.; Nishimura, H.; Wakamiya, A.; Tachibana, Y. Photo-Excitation Intensity Dependent Electron and Hole Injections from Lead Iodide Perovskite to Nanocrystalline TiO_2 and Spiro-OMeTAD. *Chem. Commun.* **2016**, *52*, 673–676.
3. Vivo, P.; Salunke, J. K.; Priimagi, A. Hole-Transporting Materials for Printable Perovskite Solar Cells. *Materials* **2017**, *10*, 1087.
4. Yu, Z.; Sun, L. Recent Progress on Hole-Transporting Materials for Emerging Organometal Halide Perovskite Solar Cells. *Adv. Energy Mater.* **2015**, *5*, 1500213.
5. Yao, Z.; Zhang, F.; Guo, Y.; Wu, H.; He, L.; Liu, Z.; Cai, B.; Guo, Y.; Brett, C. J.; Li, Y.; Srambickal, C. V.; Yang, X.; Chen, G.; Widengren, J.; Liu, D.; Gardner, J. M.; Kloo, L.; Sun, L. Conformational and Compositional Tuning of Phenanthrocarbazole-Based Dopant-Free Hole-Transport Polymers Boosting the Performance of Perovskite Solar Cells. *J. Am. Chem. Soc.* **2020**, *142*, 17681–17692.
6. Zhang, F.; Yao, Z.; Guo, Y.; Li, Y.; Bergstrand, J.; Brett, C. J.; Cai, B.; Hajian, A.; Guo, Y.; Yang, X.; Gardner, J. M.; Widengren, J.; Roth, S. V.; Kloo, L.; Sun, L. Polymeric, Cost-Effective, Dopant-Free Hole Transport Materials for Efficient and Stable Perovskite Solar Cells. *J. Am. Chem. Soc.* **2019**, *141*, 19700–19707.
7. Lee, J.; Byranvand, M. M.; Kang, G.; Son, S. Y.; Song, S.; Kim, G.; Park, T. Orcid, Green-Solvent-Processable, Dopant-Free Hole-Transporting Materials for Robust and Efficient Perovskite Solar Cells. *J. Am. Chem. Soc.* **2017**, *139*, 12175–12181.
8. Chen, H.; Huang, T.; Chang, T.; Sanehira, Y.; Kung, C. W.; Chu, C.; Ikegami, M.; Miyasaka, T.; Ho, K. Efficiency Enhancement of Hybrid Perovskite Solar Cells with MEH-PPV Hole-Transporting Layers. *Sci. Rep.* **2016**, *6*, 34319.
9. Zhang, Z.; Liang, L.; Deng, L.; Ren, L.; Zhao, N.; Huang, J.; Yu, Y.; Gao, P. Fused Dithienopicenocarbazole Enabling High Mobility Dopant-Free Hole-Transporting Polymers for Efficient and Stable Perovskite Solar Cells. *ACS Appl. Mater. Interfaces* **2021**, *13*, 6688–6698.
10. Cetin, C.; Chen, P.; Hao, M.; He, D.; Bai, Y.; Lyu, M.; Yun, J.; Wang, L. Inorganic p-Type Semiconductors as Hole Conductor Building Blocks for Robust Perovskite Solar Cells. *Adv. Sustain. Syst.* **2018**, *2*, 1800032.
11. You, G.; Liu, L.; Wang, J.; Zhao, M.; Zhao, C.; Cai, X.; Tang, J.; Lu, F.; Jiu, T. Tris(pentafluorophenyl)borane-Modified P3CT-K as an Efficient Hole-Transport Layer for Inverted

Planar $MAPbI_3$ Perovskite Solar Cells. *Adv. Sustain. Syst.* **2021**, *5*, 2100107.
12. Bi, D.; Xu, B.; Gao, P.; Sun, L.; Graetzel, M.; Hagfeldt, A. Facile Synthesized Organic Hole Transporting Material for Perovskite Solar Cell with Efficiency of 19.8%. *Nano Energy* **2016**, *23*, 138–144.
13. Bera, S.; Hu, X. Nickel-Catalyzed Regioselective Hydroalkylation and Hydroarylation of Alkenyl Boronic Esters. *Angew. Chem. Int. Ed.* **2019**, *58*, 13854–13859.
14. Wu, F.; Ji, Y.; Zhong, C.; Liu, Y.; Tan, L.; Zhu, L. Fluorine-Substituted Benzothiadiazole-Based Hole Transport Materials for Highly Efficient Planar Perovskite Solar Cells with FF Exceeding 80%. *Chem. Commun.* **2017**, *53*, 8719–8722.
15. Li, M.; Wu, J.; Wang, G.; Wu, B.; Sun, Z.; Xue, S.; Qiao, Q.; Liang, M. The Donor-Dependent Methoxy Effects on the Performance of Hole-Transporting Materials for Perovskite Solar Cells. *J. Energy Chem.* **2020**, *47*, 10–17.
16. Li, Z.; Zhu, Z.; Chueh, C.; Jo, S. B.; Luo, J.; Jang, S.; Jen, A. K. Y. Rational Design of Dipolar Chromophore as an Efficient Dopant-Free Hole-Transporting Material for Perovskite Solar Cells. *J. Am. Chem. Soc.* **2016**, *138*, 11833–11839.
17. Zhang, H.; Liu, K.; Wu, K.; Chen, Y.; Deng, R.; Li, X.; Jin, H.; Li, S.; Chuang, S. S. C.; Wang, C. Hydrogen-Bonding-Mediated Solid-State Self-Assembled Isoepindolidones (isoEpi) Crystal for Organic Field Effect Transistor. *J. Phys. Chem. C* **2018**, *122*, 5888.
18. Zhang, H.; Yang, K.; Chen, Y.; Bhatta, R.; Tsige, M.; Cheng, S. Z. D.; Zhu, Y. Polymers Based on Benzodipyrrolidone and Naphthodipyrrolidone with Latent Hydrogen-Bonding on the Main Chain. *Macromol. Chem. Phys.* **2017**, *218*, 1600617.
19. Yao, J.; Yu, C.; Liu, Z.; Luo, H.; Yang, Y.; Zhang, G.; Zhang, D. Significant Improvement of Semiconducting Performance of the Diketopyrrolopyrrole–Quaterthiophene Conjugated Polymer through Side-Chain Engineering via Hydrogen-Bonding. *J. Am. Chem. Soc.* **2016**, *138*, 173–185.
20. Oh, J. Y.; Rondeau-Gagne, S.; Chiu, Y.; Chortos, A.; Lissel, F.; Wang, G. N.; Schroeder, B. C.; Kurosawa, T.; Lopez, J.; Katsumata, T.; Xu, J.; Zhu, C.; Gu, X.; Bae, W.; Kim, Y.; Jin, L.; Chung, J.; Tok, J. B. H.; Bao, Z. Intrinsically Stretchable and Healable Semiconducting Polymer for Organic Transistors. *Nature* **2016**, *539*, 411–145.
21. Wang, S.; Wang, Z.; Huang, Y.; Hu, Y.; Yuan, L.; Guo, S.; Zheng, L.; Chen, L.; Yang, C.; Zheng, Y.; Qi, J.; Yu, L.; Li, H.; Wang, W.; Ji, D.; Chen, X.; Li, J.; Li, L.; Hu, W. Directly Patterning Conductive Polymer Electrodes on Organic Semiconductor via In Situ Polymerization in Microchannels for High-Performance Organic Transistors. *ACS Appl. Mater. Interfaces* **2021**, *13*, 17852–17860.
22. Zhang, H.; Li, R.; Deng, Z.; Cui, S.; Wang, Y.; Zheng, M.; Yang, W. π-Conjugated Oligomers Based on Aminobenzodifuranone and Diketopyrrolopyrrole. *Dyes Pigments* **2020**, *181*, 108552.
23. Zhang, H.; Deng, R.; Wang, J.; Li, X.; Chen, Y.; Liu, K.; Taubert, C. J.; Cheng, S. Z. D.; Zhu, Y. Crystalline Organic Pigment Based Field Effect Transistors. *ACS Appl. Mater. Interfaces* **2017**, *9*, 21891–21899.
24. Kaneko, R.; Chowdhury, T.; Sugawa, K.; Lee, J.; Otsuki, J.; Islam, A. Electro-Active Nanofibers of a Tetrathiafulvalene Derivative with Amide Hydrogen Bonds as a Dopant-Free Hole Transport Material for Perovskite Solar Cells. *Solar Energy* **2019**, *194*, 248–253.
25. Mas-Montoya, M.; Gomez, P.; Curiel, D.; da Silva, I.; Wang, J.; Janssen, R. A Self-Assembled Small-Molecule-Based Hole-Transporting Material for Inverted Perovskite Solar Cells. *Chem.-Eur. J.* **2019**, *26*, 10276–10282.
26. Luo, H.; Liu, Z.; Geng, H.; Yi, Y.; Broch, K.; Hu, Y.; Sadhanala, A.; Jiang, L.; Qi, P.; Cai, Z.; Sirringhaus, H.; Zhang, D. Q. Remarkable Enhancement of Charge Carrier Mobility of Conjugated Polymer Field-Effect Transistors upon Incorporating an Ionic Additive. *Sci. Adv.* **2016**, *2*, 1600076.
27. Dong, Y.; Zhu, H.; Cao, X.; Han, Y.; Zhang, H.; Yang, Q.; Zhang, Y.; Zhao, J.; Yin, G.; Wang, S. Simple 9,10-Dihydrophenanthrene Based Hole-Tansporting Materials for Efficient Perovskite Solar Cells. *Chem. Eng. J.* **2020**, *402*, 126298.
28. Ding, X.; Wang, H.; Chen, C.; Li, H.; Tian, Y.; Li, Q.; Wu, C.; Ding, L.; Yang, X.; Cheng, M. Passivation Functionalized Phenothiazine-Based Hole Transport Material for Highly Efficient Perovskite Solar Cell with Efficiency Exceeding 22%. *Chem. Eng. J.* **2021**, *410*, 128328.
29. Wu, G.; Zhang, Y.; Kaneko, R.; Kojima, Y.; Islam, A.; Sugawa, K.; Otsuki, J.; Liu, S. Anthradithiophene Based Hole-Transport Material for Efficient and Stable Perovskite Solar Cells. *J. Energy Chem.* **2020**, *48*, 293–298.
30. Wang, Y.; Liao, Q.; Chen, J.; Huang, W.; Zhuang, X.; Tang, Y.; Li, B.; Yao, X.; Feng, X.; Zhang, X.; Su, M.; He, Z.; Marks, T.; Facchetti, A.; Guo, X. Teaching an Old Anchoring Group New Tricks: Enabling Low-Cost, Eco-Friendly Hole-Transporting Materials for Efficient and Stable Perovskite Solar Cells. *J. Am. Chem. Soc.* **2020**, *142*, 16632–16634.
31. Ke, W.; Priyanka, P.; Vegiraju, S.; Stoumpos, C.; Spanopoulos, I.; Soe, C. M. M; Marks, J.; Chen, M.; Kanatzidis, M. G. Dopant-Free Tetrakis-Triphenylamine Hole Transporting Material for Efficient Tin-Based Perovskite Solar Cells. *J. Am. Chem. Soc.* **2018**, *140*, 388–393.
32. Glowacki, E. D.; Irimia-Vladu, M.; Bauer, S.; Sariciftci, N. S. Hydrogen-Bonds in Molecular Solids—From Biological Systems to Organic Electronics. *J. Mater. Chem. B* **2013**, *1*, 3742–3753.
33. Hu, Y.; Motzer, H.; Etxeberria, A.; Fernandez-Berridi, M.; Iruin, J.; Painter, P. C.; Coleman, M. M. Concerning the Self-Association of N-Vinyl Pyrrolidone and Its Effect on the Determination of Equilibrium Constants and the Thermodynamics of Mixing. *Macromol. Chem. Phys.* **2000**, *201*, 705.
34. Kuo, S.; Chang, F. Studies of Miscibility Behavior and Hydrogen Bonding in Blends of Poly(vinylphenol) and Poly (vinylpyrrolidone). *Macromolecules* **2001**, *34*, 5224.
35. Coleman, M. M.; Skrovanek, D. J.; Hu, J.; Painter, P. C. Hydrogen Bonding in Polymer Blends. FTIR Studies of UrethaneEther Blends. *Macromolecules* **1988**, *21*, 59.
36. Zhang, H.; Tung, W.; Li, X.; Jin, H. L.; Deng, R.; Chen, Y.; Mao, Y.; Zhu, Y. Conjugated Polymer with Dynamic and Thermoreversible Hydrogen Bonding on the Backbone. *Ploymer* **2020**, *203*, 122787.

DOI: 10.31635/ccschem.021.202101483
CCS Chem. **2021**, *3*, 3309–3319

37. Rakstys, K.; Paek, S.; Gao, P.; Gratia, P.; Marszalek, T.; Grancini, G.; Cho, K.; Genevicius, K.; Jankauskas, V.; Pisula, W.; Nazeeruddin, M. K. Molecular Engineering of Face-On Oriented Dopant-Free Hole Transporting Material for Perovskite Solar Cells with 19% PCE. *J. Mater. Chem. A* **2017**, *5*, 7811–7815.
38. Guo, H.; Zhang, H.; Shen, C.; Zhang, D.; Liu, S.; Wu, Y.; Zhu, W. Coplanar π-Extended Quinoxaline Based Hole-Transporting Material Enabling over 21% Efficiency for Dopant-Free Perovskite Solar Cells. *Angew. Chem. Int. Ed.* **2021**, *60*, 2674–2680.
39. Li, B.; Li, Z.; Xing, J.; Zhu, M.; Zhou, Z. Fused Furan-Based Organic Small Molecules as Dopant Free Hole Transporting Material for Inverted Perovskite Solar Cells. *Sol. RRL* **2020**, *4*, 2000536.
40. Cao, J.; Liu, Y.; Jing, X.; Yin, J; Li, J.; Xu, B.; Tan, Y.; Zheng, N. Well-Defined Thiolated Nanographene as Hole-Transporting Material for Efficient and Stable Perovskite Solar Cells. *J. Am. Chem. Soc.* **2015**, *137*, 10914–10917.
41. Liu, M.; Endo, M.; Shimazaki, A.; Wakamiya, A.; Tachibana, Y. Identifying an Optimum Perovskite Solar Cell Structure by Kinetic Analysis: Planar, Mesoporous Based, or Extremely Thin Absorber Structure. *ACS Appl. Energy Mater.* **2018**, *1*, 3722.
42. Yamada, Y.; Nakamura, T.; Endo, M.; Wakamiya, A.; Kanemitsu, Y. Photocarrier Recombination Dynamics in Perovskite $CH_3NH_3PbI_3$ for Solar Cell Applications. *J. Am. Chem. Soc.* **2014**, *136*, 11610.
43. Cai, N.; Li, F.; Chen, Y.; Luo, R.; Hu, T.; Lin, F.; Yiu, S.; Liu, D.; Lei, D.; Zhu, Z.; Jen, A. Synergistical Dipole-Dipole Interaction Induced Self-Assembly of Phenoxazine-Based Hole-Transporting Materials for Efficient and Stable Inverted Perovskite Solar Cells. *Angew. Chem. Int. Ed.* **2021**, *60*, 20437–20442.
44. Chen, Y.; Li, N.; Wang, L.; Li, L.; Xu, Z.; Jiao, H.; Liu, P.; Zhu, C.; Zai, H.; Sun, M.; Zou, W.; Zhang, S.; Xing, G.; Liu, X.; Wang, J.; Li, D.; Huang, B.; Chen, Q.; Zhou, H. Impacts of Alkaline on the Defects Property and Crystallization Kinetics in Perovskite Solar Cells. *Nat. Commun.* **2019**, *10*, 1112.

DOI: 10.31635/ccschem.021.202101483
CCS Chem. **2021**, *3*, 3309–3319